ARTICLE

Bromine Incorporation and Suppressed Cation Rotation in Mixed-Halide Perovskites

Andrew Johnston, Grant Walters, Makhsud I. Saidaminov, Ziru Huang, Koen Bertens, Niina Jalarvo, and Edward H. Sargent*

Read Online

ACCESS | Metrics & More | Article Recommendations | Supporting Information

ABSTRACT: Engineering the composition of perovskite active layers has been critical in increasing the efficiency of perovskite solar cells (PSCs) to more than 25% in the latest reports. Partial substitutions of the monovalent cation and the halogen have been adopted in the highest-performing devices, but the precise role of bromine incorporation remains incompletely explained. Here we use quasi-elastic neutron scattering (QENS) to study, as a function of the degree of bromine incorporation, the dynamics of organic cations in triple-cation lead mixed-halide perovskites. We find that the inclusion of bromine suppresses low-energy rotations of formamidinium (FA), and we find that inhibiting FA rotation correlates with a longer-lived carrier lifetime. When the fraction of bromine approaches 0.15 on the halogen site—a composition used extensively in the PSC literature—the fraction of actively rotating FA molecules is minimized: indeed, the fraction of rotating FA is suppressed by more than 25% compared to the bromine-free perovskite.

KEYWORDS: perovskites, perovskite solar cells, quasi-elastic neutron scattering, cation dynamics, energy materials
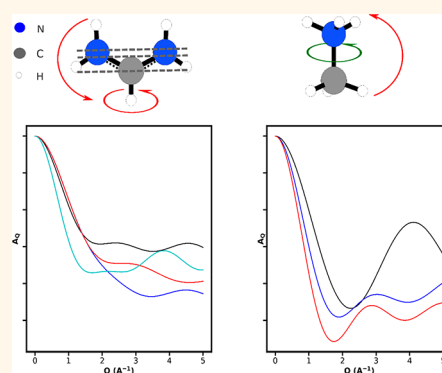
M etal halide perovskites have emerged in recent years as materials for solar cells; the AM1.5 power conversion efficiency of perovskite solar cells (PSCs) has risen to exceed 25% in only a decade.[1−6] Among the strategies employed to improve the solar conversion efficiency of PSCs, compositional engineering of the perovskite active layer has proven particularly successful.[2,7−9] Beginning with the archetypal MAPbI$_3$ perovskite, researchers modified the composition on both the A-site and X-site ions, partially substituting methylammonium (MA) with Cs and form-amidinium (FA), and partially substituting I with Br.

Notably, incorporation of 15% Br on X-sites—approximately one of every six X-sites—results in an optimum solar performance for mixed FA-MA solar cells.[2] State-of-the-art PSCs reported in the past several years have reconfirmed the 15% Br incorporation, even as other aspects of the active layer have evolved.[2,6,7,10] The approach runs counter to purely bandgap considerations: bromine moves the bandgap farther from the ideal bandgap for a single-junction solar cell. In addition, the mobility of CsFA perovskites decreases with increasing bromine content.[11] Halide segregation introduces stability issues,[12−14] so understanding the physical origins of the improved PCE, and ultimately using these insights to find more stable results to high performance, is an important goal for the field. The precise role of bromine—and the optimum at 15% incorporation—in mixed-halide devices remains unanswered despite its wide use.

When 15% bromine is incorporated, ~1/6th of the iodine atoms are substituted with bromine. We hypothesized that interactions of the cation and the PbX$_6$ octahedron in the perovskite structure are amplified under such conditions. Iodine and bromine have different electronegativities and different hydrogen-bonding strengths,[15,16] and therefore the positively charged A-site cation can reasonably be expected to have a preferred orientation toward one of the halides. We suspected that if only one different halogen was present, on average, this effect would be more noticeable.

The role organic cations play in photocarrier dynamics has been the subject of debate.[15−23] It is speculated that carriers in organic−inorganic halide perovskites travel as polarons.[19] The MA cations have also been proposed to create ferroelectric domains, which screen free carriers.[18,23−25] However, other studies have shown that the reorientation of MA has negligible impact on the exciton binding energy[15,26] and the charge carrier dynamics.[15,16] The improved charge transport at lower temperatures observed in organic−inorganic halide perovskites has
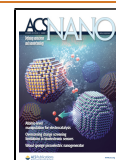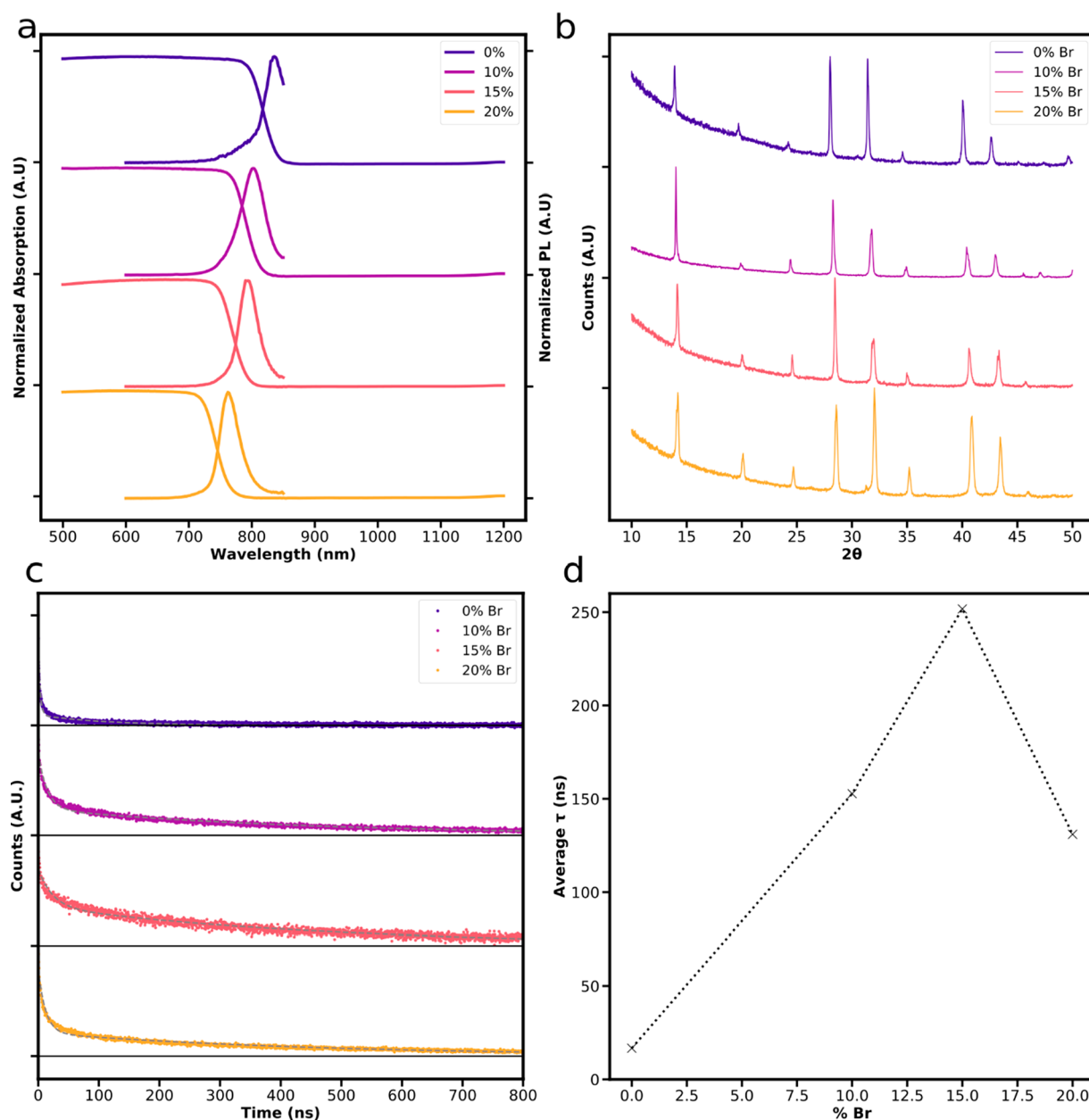
Figure 1. Photophysical and structural characterization of crushed single crystals. (a) Normalized absorption and PL spectrum of each sample. (b) XRD profiles obtained for each sample. (c) Transient PL traces of each sample measured at the peak emission wavelength. (d) Average lifetime obtained from a bi-exponential fit of each transient PL trace, as a function of Br incorporation.

instead been ascribed principally to a decrease in the intensity of longitudinal optical phonons, which were shown to couple strongly with free carriers in organic lead halide perovskites.[15,27] It has also been shown that the organic and inorganic sublattices are coupled, indicating the phonons of the inorganic lattice may be influenced by the motion of the organic cations.[28] While there have been studies that directly probe the influence of MA rotation on carrier dynamics, the influence of FA rotations on charge carriers has not been studied.[16]

Quasi-elastic neutron scattering (QENS) is a technique that has been employed previously to explore the dynamics of MA in $MAPbI_3$.[29−33] QENS offers a route to directly investigate the organic cation rotation: neutron scattering is sensitive to hydrogen, and the signal obtained from QENS can thus be attributed to motion of the hydrogen atoms, which allows us to

follow, with high specificity, the dynamics of the organic cations in the mixed-halide perovskite systems.

To eliminate the impact of variations in the crystallinity of films as a function of perovskite composition, we use single-crystal powders of triple-cation mixed-halide perovskites in which we vary Br incorporation. We found that the perovskite exhibiting the strongest suppression of FA rotation exhibits the longest carrier lifetime. We propose that FA rotation in mixed-halide perovskites contributes to the electron−phonon coupling in perovskites that is known to quench carriers.

RESULTS AND DISCUSSION

To investigate the effects of Br incorporation on organic cation dynamics in perovskites used in state-of-the-art solar cell architectures, we prepared four perovskite samples for analysis: $Cs_{0.05}FA_{0.8}MA_{0.15}Pb(I_{1−x}Br_x)_3$, where $x = 0$, 0.1, 0.15, and 0.2.
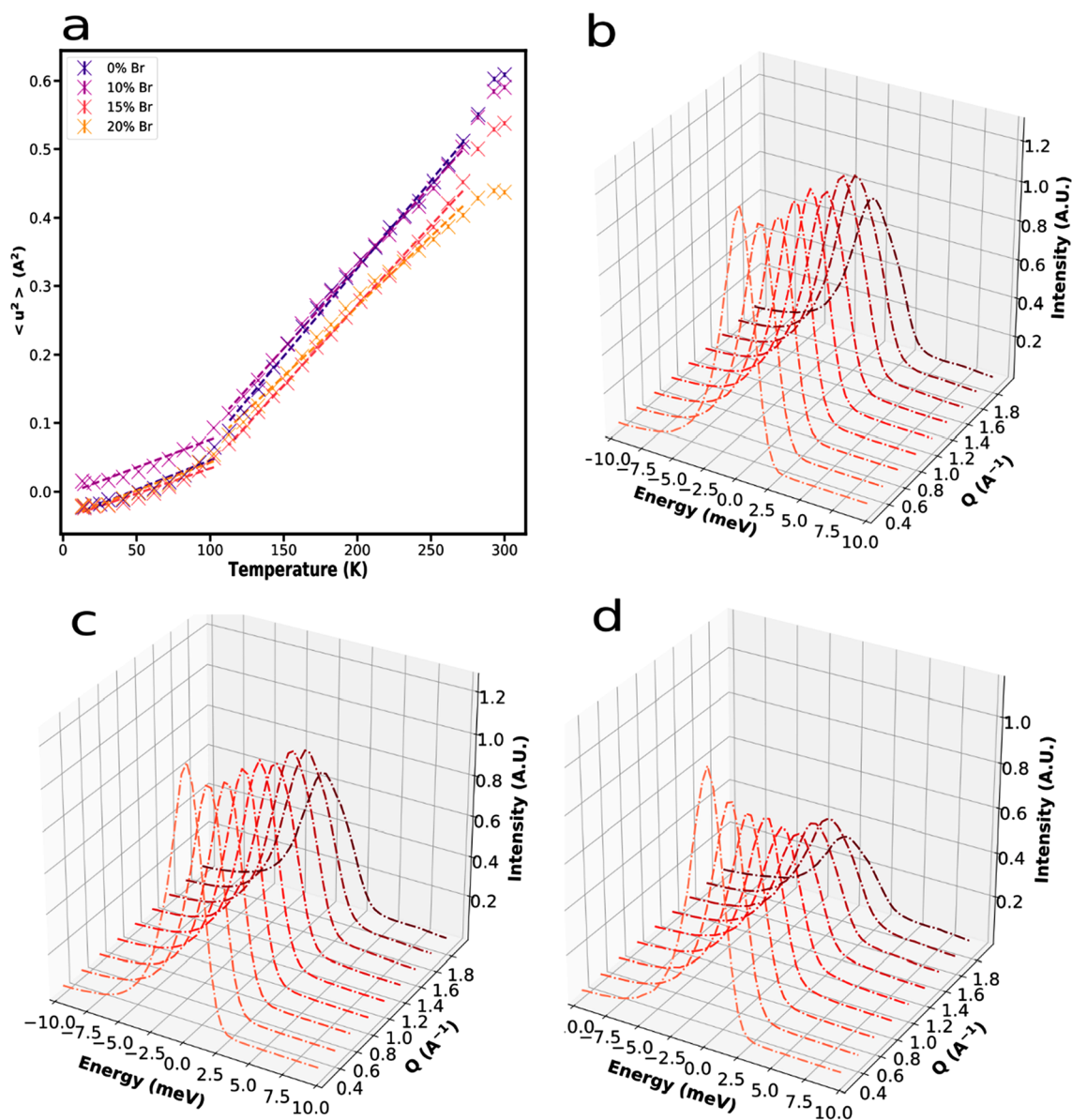
Figure 2. QENS findings for perovskite samples. (a) Mean-squared displacement of the perovskite lattice of each sample. (b–d) Intensity of the QENS signal, plotted as a function of energy transfer and momentum (Q), at (b) 80, (c) 120, and (d) 160 K for the 15% Br sample. As the temperature is increased, the signal is broadened due to increased rotations of the organic cations.

We chose this composition because the triple-cation, 15% Br system provides the most consistent baseline composition for single-junction solar cells and is used extensively in the literature.[2,6,7,10] We grew single crystals of each material (see Experimental Methods for details) and ground the sample into a powder before measuring.

Photophysical and Structural Characterization. We first measured the photophysical and structural properties of the ground single crystals (Figure 1) at room temperature. As the bromine content increases, the absorption and emission spectra blue shift (Figure 1a) as expected. The main peaks in the X-ray diffraction (XRD) profile shift to higher angles (Figure 1b); this is due to the incorporation of the smaller Br^- ion into the lattice, which decreases the lattice size. Each of the samples shows characteristic perovskite peaks at ∼14°, ∼20°, and ∼28°; we also note the absence of the characteristic δ-phase of $FAPbI_3$, which has peaks at 11.6° and 12.7°, indicating that each sample crystallized purely in the cubic phase.[7]

The powder XRD peak corresponding to the (100) crystallographic plane of the perovskite shifts from 13.98° to 14.20° when the bromine incorporation is increased from 0% to 20%. This corresponds to a change in lattice spacing of 0.098 Å, which is a difference of ∼1.54%. As a result of the very small lattice shift, we expect that the phonon modes supported by the inorganic framework of each sample are similar. Figure S1 shows that the calculated lattice constant decreases linearly with increased bromine incorporation, indicating that the crystals were successfully doped with bromine.

The transient PL signal was measured at the peak emission wavelength for each sample (Figure 1c). The signals were fit using a bi-exponential decay, and the average lifetime for each sample was calculated (Figure 1d). The average lifetime of the 15% Br sample was at least ∼2 times longer those that of the others. Both the slow and the fast components of the fit are longer in the samples containing bromine, and the 15% Br sample shows a greatly decreased fast trapping rate (Figure S2).
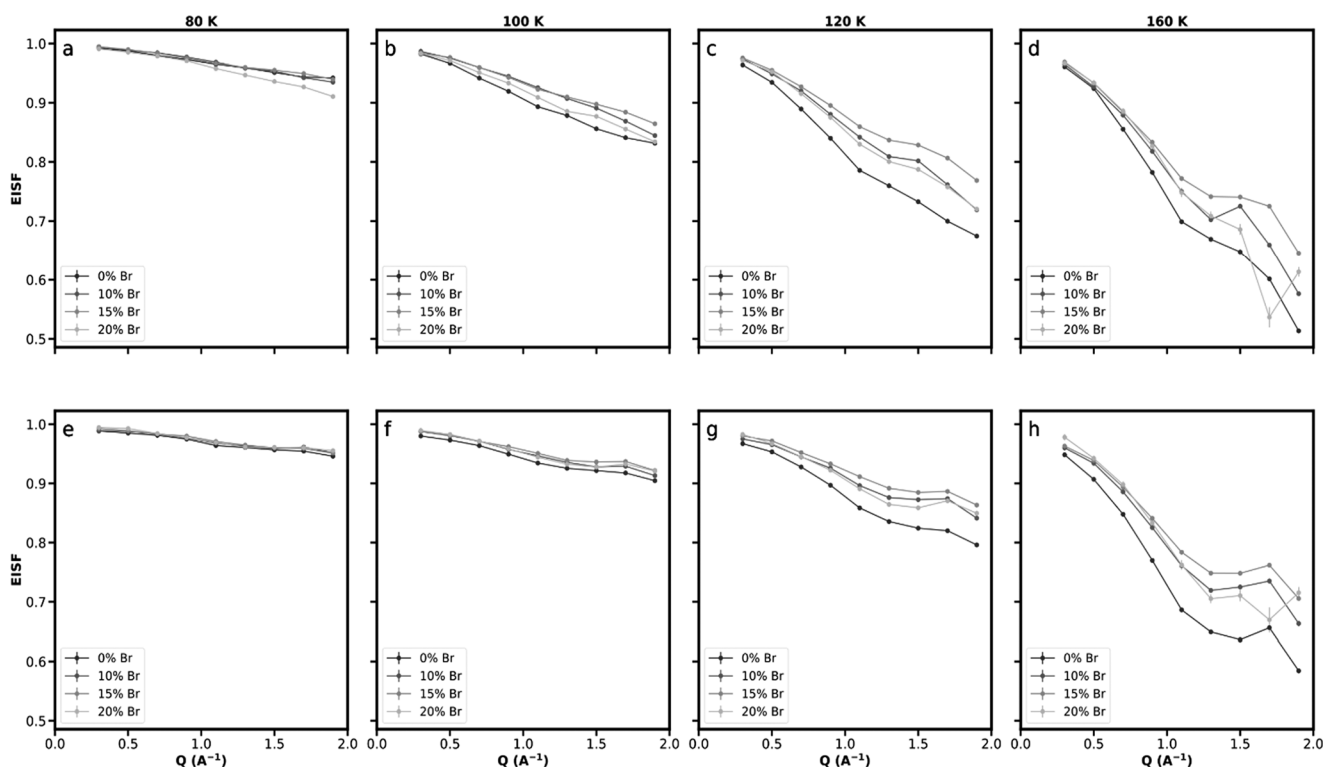
Figure 3. Calculated EISF for each sample at each temperature. (a−d) EISF calculated for the LF1 at different temperatures. (e−h) EISF for LF2. As the temperature is increased, the value of the EISF decreases as the organic cations become more energetic. The sample with 15% bromine has the highest EISF values for both LF1 and LF2. This corresponds to the smallest quasi-elastic signal and least organic cation rotation.

Increased carrier lifetime correlates with better solar cell performance,[34] since the non-radiative recombination rate has been suppressed.

Quasi-elastic Neutron Scattering Results. We employed QENS to identify the cation rotation in each sample. For each sample, we estimated the mean-squared displacement (MSD) of the lattice as a function of temperature, and the results are shown in Figure 2a. The MSD provides information relating to the rigidity possessed by the cations,[35] and the slope of the MSD as a function of temperature provides a mean force constant that describes the motion of the organic cations relative to their equilibrium positions.[36]

Below 100 K, the $FAPbI_3$ perovskite is in a hexagonal phase (space group $P6_3/mmc$), whereas above this temperature the perovskite is in a different hexagonal phase (space group $P6_3/m$, Figure S3).[37] The phase transition is seen in the MSD: the slope of each sample changes perceptibly after 100 K, indicating that the force holding the cations in place increases at lower temperatures.[36] After 270 K another transition begins, likely to the cubic phase. The onset temperature for phase transitions in $FAPbI_3$ has a strong thermal hysteresis: we note here that the samples were cooled rather than heated, and so the temperature at which transitions of cubic to hexagonal phases occur is 290 K.[37] The incorporation of MA should serve to stabilize the cubic phase at room temperature.[38] The MSD decreases as the bromine concentration increases, and the discrepancy becomes more prominent at higher temperatures. This indicates that the lattice becomes more rigid with increasing bromine. The MSD can be extracted from short measurements, as only the elastic peak intensity is extracted (Experimental Methods). To understand the cation dynamics in detail for each sample,

longer measurements with sufficient statistics to model the entire QENS spectra were collected at different temperatures.

For this purpose, we collected QENS spectra at four temperatures: 80, 100, 120, and 160 K. We sought to probe the dynamics of both hexagonal phases of the perovskite, but the cubic phase was at a temperature at which the QENS signal would be outside of the measured energy window. We note that the analysis at room temperature would be similar to the analysis at low temperature, with the cubic space group ($Pm\bar{3}m$) being used rather than the hexagonal.[39]

The intensity obtained for the 15% Br sample is shown in Figure 2b−d for 80, 120, and 160 K. The intensity decreases at higher temperatures, and likewise decreases with increasing momentum transfer. The data were fit to a sum of a Gaussian function, two Lorentzian functions, and a baseline, each of which was convolved with the resolution of the instrument, obtained by measuring each sample at 10 K (Figure S4 and Experimental Methods).

The spatial and energetic dependence of the signal from QENS can be mapped to the dynamics of molecules using the elastic incoherent structure factor (EISF). Experimentally, the EISF can be calculated for each Lorentzian fit to the data. For each momentum (Q), the relative area of the Gaussian function (corresponding to the elastic signal) is divided by the total sum of the Gaussian function and the Lorentzian function (corresponding to the quasi-elastic signal). The shape of this EISF can be compared to the theoretical ones given by the symmetry of the molecule and the crystal in which it resides (Experimental Methods).[29,40]

As a result, the shape of the EISF can be used to identify the type of motion that an organic molecule undergoes in a crystal lattice; the magnitude of the EISF can be used to determine the
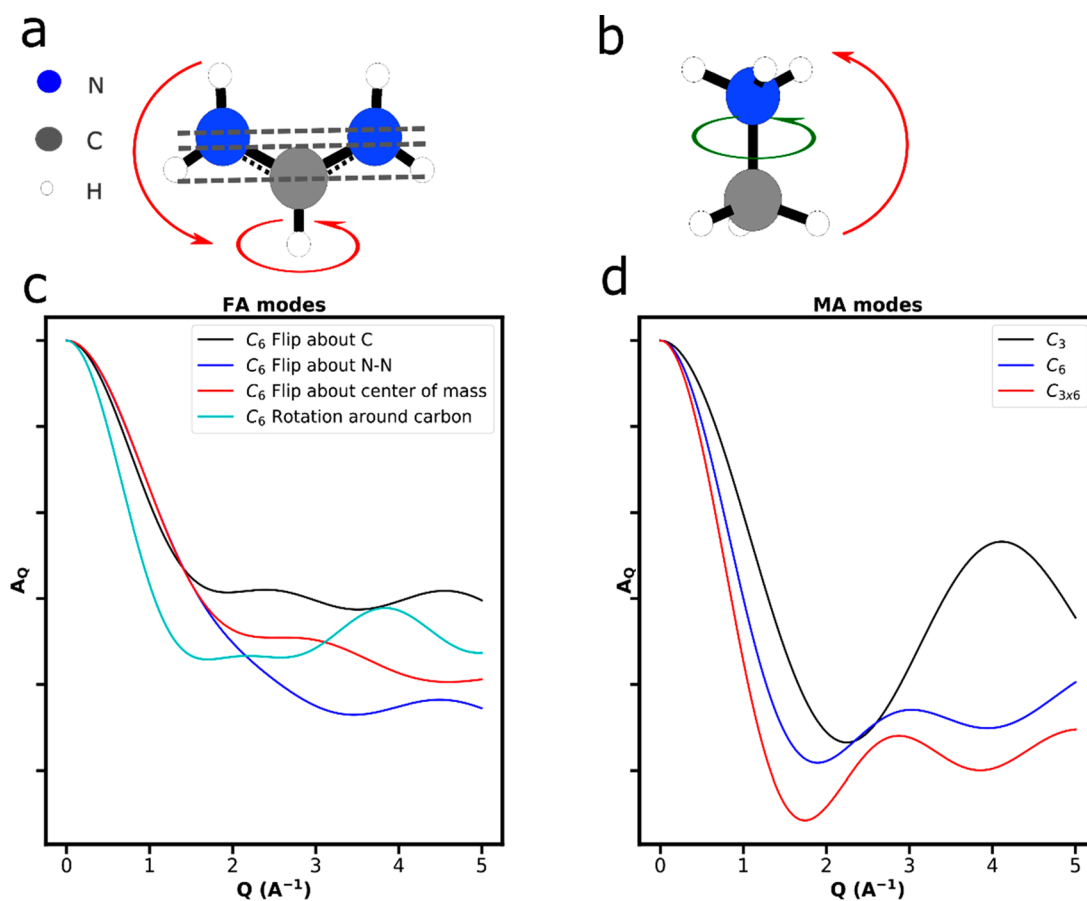
Figure 4. Possible rotations of (a) FA and (b) MA molecules. The green arrow indicates a C_3 rotation. The red arrows indicate a C_6 rotation. The gray dashed line represents the possible centers for the C_6 rotation of the FA molecule. The calculated EISF modes for (c) FA and (d) MA. We considered that each FA molecule was only undergoing one possible rotation, although different FA molecules may be undergoing different motions.

fraction of organic molecules that undergo the motion it describes.

Ideally, each separate Lorentzian function should correspond to a single motion: here, the fitting of additional Lorentzian functions did not improve the overall fit, two were found to be sufficient to model the spectra. As we discuss further below, there are more than two distinct rotations that are possible in this crystal structure. We expected that with better experimental resolution and longer collection times the addition of more Lorentzian functions would improve the fit. To account for the additional motions present, we also allowed each Lorentzian to represent a combination of motions in our models.

We extracted the EISF for each sample at each temperature (Figure 3). For each sample, the data were fit with two Lorentzian functions (Figure S4), in which one Lorentzian was narrow (**LF1**, Figure 3a−d), and one Lorentzian was broad (**LF2**, Figure 3e−h). The EISFs have similar magnitudes, which indicates that the motions described by the two Lorentzian functions contribute similarly to the total incoherent scattering. The EISFs have different shapes, which indicate that they describe distinct motions.

The EISF decreases—i.e., there is a larger quasi-elastic signal and more dynamics become observable—with increasing temperature. The relative increase in the amount of quasi-elastic scattering is most pronounced when the temperature changes from 100 to 120 K, especially for the **LF1** (Figure 3b,c). In MAPbI$_3$, the phase change from orthorhombic to tetragonal

results in activation of the C_4 rotation of the MA;[29] here, the phase change from one hexagonal phase to another that each samples undergoes at ∼100 K results in a similar phenomenon, although it is less pronounced.

At each temperature, the 15% Br sample exhibits the highest EISF. This indicates that the sample with 15% Br has the lowest amount of quasi-elastic scattering and thus has the least active cations. The suppression of organic cation motion, as a function of bromine incorporation, corresponds with the reported trend of PSC performance as a function of bromine incorporation. This becomes more prominent at higher temperatures and at higher Q.

To understand which type of motion is suppressed, we sought to fit the measured EISFs with the theoretical EISFs for each molecule.

Analysis of Dynamics. The possible rotations of the hydrogens in the two organic molecules, FA and MA, are given in Figure 4a,b. The hydrogens in MA may rotate about the C−N bond, and the entire molecule may rotate within the crystal structure. The dynamics of MA have been studied with QENS previously.[29−31] We note that here, the symmetry of the local crystal environment is hexagonal rather than tetragonal at the measured temperatures due to the presence of FA, and so the rotations are characterized by the C_6 point group rather than the C_4 point group. The resonant double bond in the FA ion prevents the rotation of hydrogen atoms about either C−N bonds, and as such the only possible rotation of hydrogen atoms
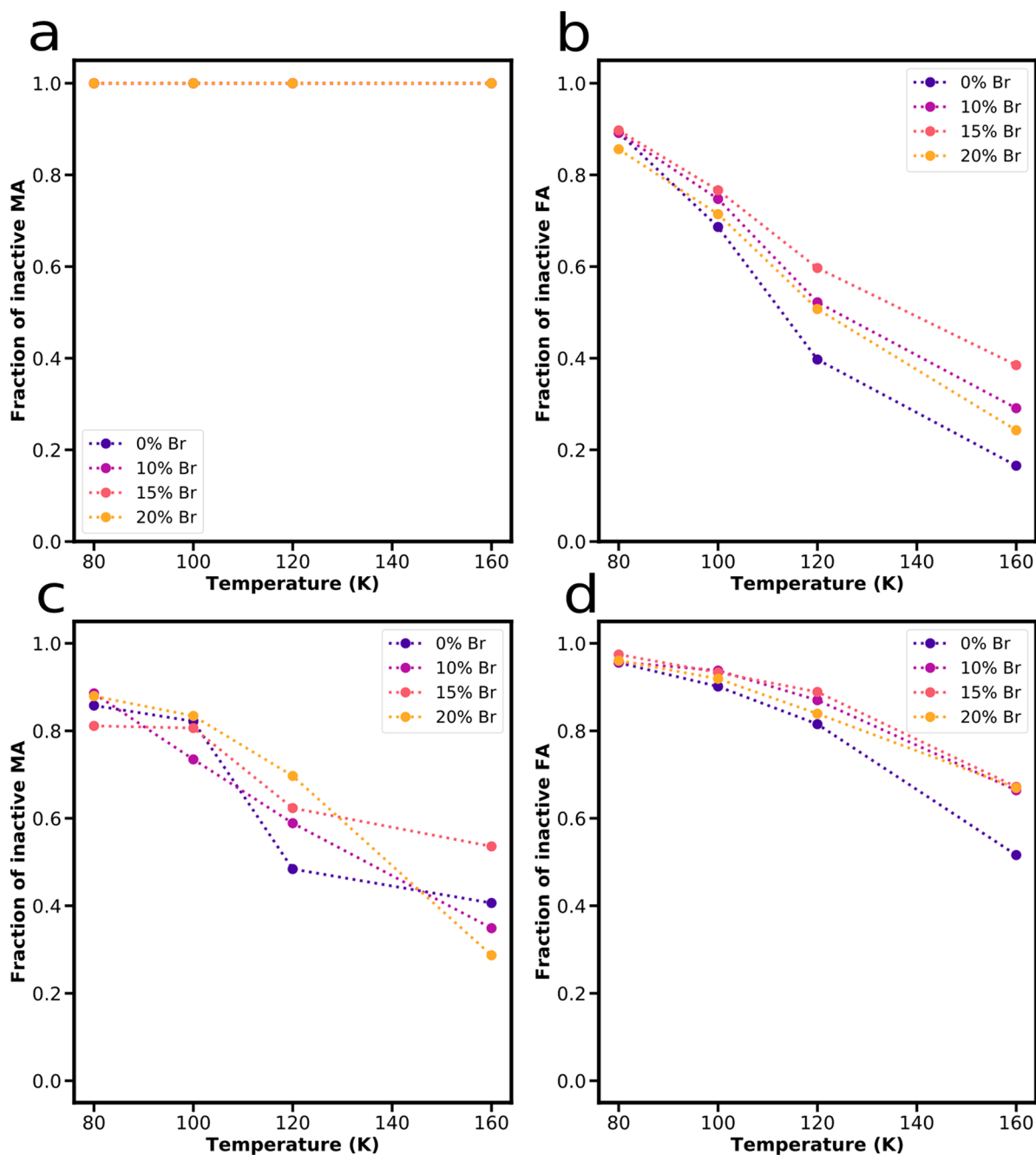
Figure 5. Fraction of cations active at each temperature. (a, b) Relative fractions of MA and FA that contribute to LF1. (c, d) Relative fractions of MA and FA that contribute to LF2. Interestingly, the 15% Br sample shows the greatest reduction in the fraction of cations undergoing the FA. The fraction of inactive FA correlates with the PL lifetimes, indicating that FA rotation may quench photoexcited carriers.

is that of the entire molecule. We identified four different rotations that the FA molecule is most likely to undergo: the molecule can flip about the carbon atom; the molecule can flip about the N−N axis; the molecule can flip about its center of mass; or the molecule can rotate about the carbon−hydrogen bond. The dynamics of pure FAPbI$_3$ were recently investigated with ultrafast spectroscopy, and the flipping mode of FA about the N−N axis was found to be dominant.[41]

We used jump models[29,40] to calculate the different modes of the EISF based on the rotations of each molecule. The EISF for a given molecule can be described by

$$A_\gamma = \frac{X_\mu^{E e}}{g} \sum_\nu \sum_\eta X_\mu^{\nu\eta} \sum_{C_\nu} \sum_{M_\eta} j_0(Q|R - C_\nu M_\eta R|) \tag{1}$$

in which j_0 is the zeroth-order Bessel function and $|R - C_\nu M_\eta R|$ is the distance traveled for a given rotation. γ runs over all the irreducible representations of the direct product of the local crystal environment, **C**, and that of the molecule, **M**. g is the order of γ and the sums over α and β run over all the classes of **C** and **M**, respectively. The sums of C_α and M_β run over all rotations that belong to the crystal class, α, and the molecular class, β, respectively.[29] $X_\mu^{\nu\eta}$ are the products of the products of the characters of $C_{\gamma C}$ and $M_{\gamma M}$, $X_{\gamma C}^\alpha$ and $X_{\gamma M}^\beta$, respectively: $X_\mu^{\nu\eta} =$

$X^{\alpha}_{\gamma C} X^{\beta}_{\gamma M}$.[29,40] We note that the jump models do not depend on temperature.

We calculated the distance each hydrogen in the molecule travels for both FA and MA under each of their respective rotations, and the distances are tabulated in Tables S1 and S2, respectively. The atomic positions were obtained from CIF files of FAI (CCDC: 1538402)[42] and MAPbI$_3$ (CCDC: 1470054).[43] Two-dimensional projections of each molecule under each rotation are depicted in the Figures S5 (FA) and S6 (MA). The resulting EISF modes for each type of rotation under consideration are depicted for FA in Figure 4c and for MA in Figure 4d. Interestingly, the MA molecule exhibits the most quasi-elastic scattering under its combined rotations; despite only having 15% MA, it is possible that the total signal of each sample will be greatly influenced by the motion of MA.

We fit the experimental EISF according to the following equation:

$$1 - \sum_{i=1}^{N} x_i (1 - A_{i,0}(Q)) \tag{2}$$

in which $A_{i,0}(Q)$ is the theoretical EISF for a given type of rotation i, x_i is the fraction of hydrogens active for a particular EISF, and N is the number of rotations considered.[32] We fit every combination of an FA mode and either C$_3$ or C$_3 \otimes$ C$_6$ MA modes for each sample at each temperature. We constrained the fraction of hydrogens that were available to rotate in each case based on the stoichiometry of the perovskite: 18.3% of the hydrogens are MA, and 81.6% are FA. The results of the fits, obtained using a least-squares method, are given in Tables S3 (**LF1**) and S4 (**LF2**). For **LF1**, excellent fits are given when considering the FA C$_6$ flip about the N−N axis, considering no MA rotations at all. This is the dominant mode of rotation, and agrees with previous reports.[41]

For **LF2**, the best fits are obtained when considering both MA and FA. The best fits are obtained when the MA C$_3$ mode and the FA C$_6$ rotation about the carbon mode are combined: in MAPbI$_3$ the C$_4$ rotation only activates at 165 K when the phase changes,[29] and as transitions to higher symmetry phases do not occur until higher temperatures in FA-perovskites,[37] it is expected that the C$_6$ rotation of MA is inhibited at the temperatures studied in this report.

We obtained higher temperature QENS data on pure FAPbBr and MAPbBr and estimated the activation energy of the different motions by fitting the full width at half-maximum (fwhm) of the Lorentzians to an Arrhenius equation (Figure S7).[32] We calculate the activation energy of the FA rotation to be 47 meV, while the MA activation energies are 15 and 76 meV for the two different motions, respectively. **LF1** has a narrower fwhm than **LF2**, indicating that it describes a motion with higher energy,[29] which is consistent with it only being associated with the FA motion, rather than both MA C$_3$ and FA.

The fraction of each cation that is *inactive* is shown in Figure 5: the top row shows the fraction that corresponds to **LF1**, and the bottom row corresponds to **LF2**. As expected from the EISFs, the 15% Br sample has the lowest active fraction of rotating cation.

We sought to determine if the suppressed cation motion was correlated with the photophysical properties of the perovskite at the temperatures at which we performed the measurement, and so we measured the PL and transient PL at each of the temperatures at which we collected QENS data. The data are shown in Figures S8 (PL) and S9 (PL lifetimes) and are summarized in Table 1 and visualized in Figures S10−S12. To measure the PL and PL decay in the cryostat requires coupling

Table 1. Summary of the Photophysical Response and Cation Immobilization at Each Temperature

	τ_{av} (ns)	normalized PL intensity	fraction FA immobilized	fraction MA immobilized
		80 K		
0% Br	115 ± 2	0.91	0.89 ± 0.00	0.83 ± 0.01
10% Br	89 ± 1	0.78	0.89 ± 0.00	0.86 ± 0.01
15% Br	171 ± 2	0.83	0.89 ± 0.00	0.77 ± 0.01
20% Br	120 ± 1	0.77	0.85 ± 0.01	0.85 ± 0.01
		100 K		
0% Br	71 ± 2	1.00	0.68 ± 0.01	0.78 ± 0.02
10% Br	90 ± 1	1.00	0.74 ± 0.01	0.68 ± 0.01
15% Br	139 ± 1	1.00	0.76 ± 0.00	0.76 ± 0.01
20% Br	101 ± 1	1.00	0.71 ± 0.01	0.78 ± 0.01
		120 K		
0% Br	−	0.37	0.39 ± 0.01	0.37 ± 0.07
10% Br	84 ± 1	0.29	0.51 ± 0.01	0.50 ± 0.03
15% Br	138 ± 2	0.63	0.59 ± 0.01	0.54 ± 0.02
20% Br	86 ± 1	0.63	0.50 ± 0.01	0.63 ± 0.02
		160 K		
0% Br	−	0.26	0.15 ± 0.02	0.27 ± 0.06
10% Br	−	0.14	0.28 ± 0.03	0.20 ± 0.06
15% Br	−	0.26	0.37 ± 0.02	0.43 ± 0.05
20% Br	−	0.15	0.23 ± 0.03	0.13 ± 0.07

the excitation and detection sources back to the detector, resulting in a significant decrease in the S/N ratio. When measuring lifetimes, a lower repetition rate of laser pulses is necessary, and as such we were unable to measure lifetimes for any of the samples at 160 K. At 120 K, the signal from the 0% Br sample was too weak to be measured with the same laser repetition rate as the rest of the measurements, and, as a result, the data point is excluded from further discussion. The integrated intensities of the PL spectrum are shown in Figure S8, normalized to the PL intensity at 100 K. The normalized intensities are also shown in Table 1.

At higher temperatures the 15% Br sample exhibits the longest carrier lifetime and the highest relative PL intensity. We find that longer lifetime generally correlates with the fraction of FA that is immobilized in each sample. We postulate that the phonons due to FA rotation may couple to generated electrons and increase in non-radiative recombination. We observe no correlation between the PL lifetimes or the PL intensities with MA immobilization, a finding consistent with prior reports.[16] We recently showed that MA assists in transporting charges across grain boundaries of perovskite films, indicating that the effect of MA incorporation is only observed in thin films of perovskites.[44] As a result, we expect these findings to be applicable to pure CsFA perovskites as well. We acknowledge that proving the causation of FA rotation impacting carrier dynamics is a consideration of future work; here, we only report the correlation and speculate as to its origin.

Since bromine forms stronger hydrogen bonds than iodine, the suppression of the rotation of cations due to bromine incorporation can be accounted for with a plausible physical

explanation: when there exists one Br on average in each PbX_6 octahedron, the FA cation has a preferred orientation.

In FA-perovskite, FA cation is in icosahedral coordination. When more one Br atom is present in each PbX_6 octahedra, the FA icosahedra vertices consist of ten I and two Br; the two Br atoms may anchor two FA sites available for hydrogen bonding (two hydrogen atoms on each site). As a result, the FA has a preferred orientation in the 15% Br system. But when more than one Br atom is present in each PbX_6 octahedra, the cation may have no preferred orientation, and this will on average increase its motion.

To estimate the fraction of octahedra in a perovskite crystal that have a given number of bromine atoms incorporated, we used statistical sampling to model perovskite structures with different bromine incorporation. As the bromine incorporation is increased, both the powder XRD and steady-state PL spectra show a gradual change in peak position (Figure 1), indicating that the bromine is being distributed evenly in the lattice. If there were domains of both Br-poor and Br-rich perovskite, we would expect to see the emission from the Br-rich regions being quenched by the Br-poor regions; and appreciable splitting of the powder XRD peaks to Br- and I-perovskite. As we do not observe either of these phenomena, we conclude that the bromine is distributed evenly throughout the lattice.

As a result, we randomly substitute iodine with bromine in the model perovskite structure, and count the number of bromine atoms in each octahedron. As expected, we find that on average, 10% Br incorporation results in 0.6 Br/octahedron, 15% Br leads to 0.9 Br/octahedron, and 20% leads to 1.2 Br/octahedron (Figures S14−S16). The distributions shown in Figure S13 indicate that the 15% Br sample has the largest fraction of octahedra with 1 Br.

Prior work from the Bakulin group has shown that when a mixture of Br and I are incorporated into the perovskite lattice, the rotation of organic cations is slower than when the pure halide (either Br or I) is used.[22,45] Our findings corroborate the conclusions from these works and further support the claim that it is not simply the hydrogen bond strength that determines the rotational frequency of the organic cations: if it were, simply increasing the bromine content would decrease the average cation rotation.

It is apparent that adding any bromine inhibits the rotation of the FA cation (Figure 5b,d). Recent record devices incorporate ~5% Br into the perovskite structure.[6,46] This likely inhibits the FA C_6 rotation substantially and to a lesser extent the FA C_6 flipping. However, the lower bandgap means that more solar photon fluence is turned into J_{sc}, and the improved photocurrent outweighs the slight increase in phonons due to the FA flipping rotation.

We focused here on perovskite systems in which the Br content varied from 0 to 20%, as these compositions are relevant to record single-junction PSCs. A subject of future work is identifying if the same trends can be expected in systems in which the I content is varied from 0 to 20%.

Previous studies have shown that $FAPbBr_3$ and $FAPbI_3$ have similar rotational times.[41,47] In single halide systems, no preferred orientations exist in which the strength of hydrogen bonding is greater than in the other orientations.

Carrier lifetime is also dependent on exciton binding energy, which is a function of the dielectric screening of the generated carriers.[26] In $MAPbI_3$ perovskites, a step-like change in the measured exciton binding energy at the phase change boundary indicates that the activation of the C_4 reorientation of MA

impacts the electron binding energy,[48,49] but due to the associated change in bandgap with the phase transition, it is difficult to isolate the cause of the change in binding energy.[15] While FA rotations in $FAPbI_3$ do not form long-lived ferroelectric domains,[41] we nonetheless sought to compare the exciton binding energies of the samples to determine if they were the cause of the observed differences in PL lifetimes. We measured the temperature-dependent absorption spectra of each sample (Figure S13) and fit the exciton binding energies using Elliot's theory.[48,50] The exciton binding energies obtained are very low (~2−5 meV, Table S6) as reported for $MAPbI_3$ previously.[48] The 15% Br has the highest exciton binding energies over the temperature range. As noted from the absorption spectra, there is little change with temperature, which is consistent with the relatively small shift in PL emission position with temperature (Figure 1a). We note that Elliot's theory does not model higher energies of inorganic−organic perovskites well due to assumptions in the model,[51,52] and thus only use it to compare binding energies qualitatively. Since we find no obvious trend between exciton binding energy and lifetime or relative PL intensity, we conclude that the exciton binding energy alone cannot completely explain the observed trend in photoluminescence lifetime.

To determine if the trends observed in single crystals translate to perovskite thin films, we fabricated thin films of identical composition to the single crystals. Powder XRD indicates that the thin films are predominantly in the cubic phase (Figure S17). Using X-ray photoelectron spectroscopy (XPS), we quantified the final incorporation of bromine in each sample (Table S7) and find that the bromine incorporation was slightly less than in the starting precursor solution. We measured the steady-state (Figure S18) and transient PL spectra (Figure S19) of each thin film at room temperature and found that the 10% (final incorporation = 9.5%) and 15% (13.5%) Br samples exhibited the longest lifetimes, which were improved by a factor of ~2 compared to the pure I sample. This indicates that the results obtained from the single crystals are applicable to thin films at room temperature as well.

CONCLUSIONS

We used QENS to identify the dynamics of cations in state-of-the-art triple-cation mixed-halide perovskites. In view of the superior solar cell performance of the devices incorporating 15% Br, we compared the photophysics of triple-cation mixed-halide perovskite crystals with varied Br contents and noticed that the longest lifetime was found when the Br content was 15%. We hypothesized that this may be due to an interaction with the organic cations that are present in the perovskite crystal; with QENS, we identified that when the Br content is 15%, the dynamics of the cations, particularly FA, are suppressed. We attribute this to 15% Br being the ratio at which approximately one in every six halide sites is Br, which results in a preferred orientation of the cation. This work studies the organic cation dynamics of triple-cation perovskites with QENS and correlates the dynamics with the lifetime of photogenerated carriers.

EXPERIMENTAL METHODS

Single-Crystal Growth. The single crystals were grown using the inverse crystallization method, as reported elsewhere.[53] First, 1 M solutions of $FA_{0.85}MA_{0.1}Cs_{0.05}PbI_{3-x}Br_x$ ($x = 0, 0.6$) were prepared by dissolving the constituent precursor salts in γ-butyrolactone, and portions of the resulting precursor solutions were mixed to obtain solutions with 10% and 15% Br concentration, respectively. The

solutions were filtered and then heated to 120 °C. The solutions were left at this temperature for 3 h to allow crystals to fully grow. The obtained crystals were then cleaned with isopropyl alcohol.

We attempted crystal growth using the antisolvent method but were unsuccessful (Table S8).

Optical Characterization. Optical absorption spectra were measured with a PerkinElmer 950 UV/vis/NIR spectrometer equipped with an integrating sphere for thin-film measurements. PL spectra and PL-decay measurements were carried out using a Horiba FluoroLog-3 spectrofluorometer in reflection geometry under ambient conditions. The sample was excited using monochromated light (375 nm) from a xenon lamp. The emission was passed through a 500 nm blaze grating monochromator (iHR320) and collected by an infrared photo-multiplier tube. For transient-PL measurements, the sample was excited with a 374 nm diode laser at a repetition rate of 10 MHz.

Powder XRD. The nanocrystals were drop cast onto a glass slide for measurement. XRD measurements were conducted using a Rigaku MiniFlex-6G 600 instrument (Bragg−Brentano geometry) equipped with D/teX Ultra silicon strip detector and a Cu Kα radiation source (λ = 1.5406 Å) operating at a voltage of 40 kV and a current of 15 mA.

XPS. Perovskite films were prepared on an ITO substrate. The samples were mounted on a stainless-steel mounting plate. XPS measurements were performed with the Thermo Scientific K-Alpha system. An Al Kα source was used, and the takeoff angle was 90°. To account for sample charging, the XPS spectra were calibrated to the C 1s peak at 284.8 eV.

QENS. The QENS measurements were performed at the back-scattering spectrometer BASIS[54] at the Spallation Neutron Source at the Oak Ridge National Laboratory. Si(111) analyzers were used along with neutron beam with 6.4 Å center wavelength and the incident bandwidth choppers with 60 Hz frequency. With this instrument configuration, the elastic energy resolution is 3.6 μeV (at fwhm), and the energy transfer window of ±100 μeV can be used. Samples were placed into sealed cylindrical annular aluminum containers, each one in the amount yielding to transmission probability of about 95%. Short measurements were taken every 10 K (between 10 and 300 K) to obtain diagnostic information about the dynamics in the samples. Longer scans with adequate statistics for detailed analysis of the quasi-elastic spectra were then taken at temperatures between 80 and 160 K. To determine the instrumental resolution function, each sample was cooled down to 10 K, where all the diffusive motions are essentially frozen. Data reduction was done by using Mantid package.[55]

For each sample, the elastic incoherent neutron scattering (EINS) contribution was extracted from the full spectra by integrating the elastic peak. A quantity of interest, the average mean-squared displacement (MSD or $\langle u^2 \rangle$), can be obtained by using Gaussian approximation,

$$S_{el}(Q) = A \, e^{-Q^2 \langle u^2 \rangle / 3} \tag{3}$$

in which S_{el} is the scattering function integrated over the energy resolution window (centered at $\omega = 0$).

Data Fitting. The data were reduced with Mantid package,[55] and the data were fit with DAVE software.[56] For each sample at each temperature, the data were integrated into nine Q bins. Each of the Q spectra were fit using four functions: a flat background, a Dirac delta function, and two Lorentzian functions (Figure S4). Each of these functions was convolved with the instrument resolution function, which was obtained by measuring each sample at 10 K. The functions were chosen according to the general expression for the dynamic structure factor:[40]

$$S(Q, w) = A_0(Q)\delta(\omega) + \sum_{i=1}^{N} A_i(Q)L_i(\omega) \tag{4}$$

in which

$$A_0 = a_0(Q) \, e^{-\langle u^2 \rangle Q^2} \tag{5}$$

and

$$L_i = \frac{\frac{1}{\pi}\tau_i}{1 + \omega^2 \tau_i} \tag{6}$$

The term a_0 is the EISF, $\langle u^2 \rangle$ is the MSD, and τ_i is the average jump time for a given rotation. The elastic incoherent structure factor is a measurable quantity, defined as the fraction of the total quasi-elastic intensity contained in the purely elastic peak. Thus, for each Lorentzian function, the EISF for the type of motion described by this Lorentzian can be obtained by taking the ratio of the integrated intensity of the Dirac delta function (elastic) to the sum of the integrated intensities of the Lorentzian (inelastic) and the Dirac delta function (elastic). Qualitatively, if there are more scattering events, the contribution of the inelastic signal is stronger, and the EISF will decrease. Additionally, if there is no momentum transfer ($Q = 0$), there can be no inelastic contribution and the EISF must be equal to unity. With this method, the EISF for each different type of motion (represented by each disparate Lorentzian function) is calculated. The measured EISF for each motion may be identified by comparing the shape of the EISF to the theoretical function, given in the following section.

Jump Models. In general, inelastic neutron scattering can arise from two types of motion, rotational and translational. Due to the highly ionic nature of perovskites, in the absence of applied electric fields, there should be little long-range translational motion. We thus focus on the rotational motion present in the perovskite lattice. In particular, the rotation of the dynamic cations, MA and FA, will dominate the signal. While there have been studies identifying the dynamics of MA,[29,30,32] there has to our knowledge been no work on identifying the dynamics of FA. To calculate the modes of FA and MA, we used the jump model, as described elsewhere.[29] When considering rotations about both the molecular axis and the crystal axis, the elastic and inelastic structure factors can be written as shown above in eq 1.

For the purposes of this study, it is acceptable to only consider the symmetric 1D irreducible representation of the crystal and the molecule, the structure factor derived from this representation will give the elastic incoherent structure factor.[40] The representations resulting from the product of higher representations of the crystal and molecular classes respectively give the various quasi-elastic incoherent structure factors, not discussed in this study.

There are two organic molecules under consideration: formamidinium (FA) and methylammonium (MA) (Figure 4a,b). MA, the archetypal cation for inorganic−organic halide perovskites has been characterized with QENS previously;[29,31,43] the molecule belongs to the C_3 point group: both the methyl and ammonium groups are free to rotate about the C−N bond, with a three-site occupancy. In addition, the local crystal symmetry of the FAPbI$_3$ perovskite is six-fold, belonging to the C_6 point group. There are thus 18 positions that each hydrogen atom can occupy by combining the allowed rotations under C_4 and C_3 symmetry.

The resonant double bond between the nitrogen and carbon atoms prevent hydrogen rotation about the C−N bonds in FA. As such, the only rotation possible is of the entire molecule, allowing us to only consider the local crystal symmetry, which belongs to the C_6 point group. We consider four possible C_6 rotations of FA:

- Rotation about the C atom (depicted as a rotation about the C−H bond in Figure 4a)
- Rotation parallel to an N−N axis where the axis of rotation is
  - such that the nitrogen atoms remain fixed
  - such that the center of mass of the molecule remains fixed
  - such that the carbon atom remains fixed

For the MA atom, the EISF for the combined $C_3 \otimes C_6$ rotation is given by eq 1; the character tables for the C_3 and C_6 point groups are given below:[57]

C_3 Character Table

	E	C3	(C3)
A	+1	+1	+1
E	+1	+ϵ	+ϵ
	+1	+ϵ	+ϵ

C_6 Character Table

	E	**C$_6$**	**C$_3$**	**C$_2$**	**(C$_3$)^2**	**(C$_6$)^5**
A	+1	+1	+1	+1	+1	+1
B	+1	−1	+1	−1	+1	−1
E_1	+1	+ϵ	−ϵ^*	−1	−ϵ	+ϵ^*
	+1	+ϵ^*	−ϵ	−1	−ϵ^*	+ϵ
E_2	+1	−ϵ	−ϵ	+1	−ϵ^*	−ϵ
	+1	−ϵ^*	−ϵ	+1	−ϵ	−ϵ^*

To calculate the EISF, we are only concerned with the first 1D irreducible representation: A⊗A. As the characters for all rotations for both C_3 and C_6 are 1, eq 1 is simplified. The resulting equation is an average of 18 Bessel functions of the form

$$j_0(Q|R - C_\nu M_\eta R|) \tag{7}$$

in which the distance $R - C_\nu M_\eta R$ corresponds to the total distance traveled by the hydrogen atom. Here we note that neutron scattering cross section of hydrogen is so much larger than any other atoms; it is sufficient to consider only H atoms as they dominate the signal. For any of the 18 rotations under consideration, there are six hydrogen atoms that have moved. We thus take an average of 6 Bessel functions for each combined rotation. The resulting structure factor for the combined C_3 and C_6 rotations of the MA cation can thus be expressed as

$$A_{A\otimes A} = \frac{1}{18} \sum_{C_\nu} \sum_{M_\eta} \frac{1}{6} \sum_{i=1}^{6} j_0(Q|R_i - C_\nu M_\eta R_i|) \tag{8}$$

where the distance $R_i - C_\nu M_\eta R_i$ is the distance traveled by the hydrogen atom during the combined rotations. For the FA cation, the only possible rotations are that of the entire molecule within the local crystal symmetry. The local crystal symmetry has C_6 symmetry, and thus only C_6 rotations need to be considered.

For each of MA and FA, the distances traveled by each hydrogen atom was obtained by applying a combination of standard rotation matrices to the positions of the atom. Figures S3 and S4 depict the positions of the atoms in each of the molecules projected into the $X-Z$ plane for each rotation, and Tables S1 and S2 show the distances traveled by each hydrogen after each rotation. We calculated the EISF modes shown in Figure 4c,d using these distances.

ASSOCIATED CONTENT

ⓈⒾ Supporting Information

The Supporting Information is available free of charge at https://pubs.acs.org/doi/10.1021/acsnano.0c05179.

> Figures S1−S19 and Tables S1−S8 describing in greater detail the fitting procedure for QENS data; photophysical characterization data for both the thin films and single crystals of all perovskite samples discussed in the paper; additional information on different crystal growth methods and crystal structures discussed; and numerical simulations of the number of bromine atoms in each unit cell for different bromine incorporation levels (PDF)

AUTHOR INFORMATION

Corresponding Author

> **Edward H. Sargent** − *Department of Electrical and Computer Engineering, University of Toronto, Toronto, Ontario M5S 1A4, Canada;* ⓞ orcid.org/0000-0003-0396-6495; Email: ted.sargent@utoronto.ca

Authors

> **Andrew Johnston** − *Department of Electrical and Computer Engineering, University of Toronto, Toronto, Ontario M5S 1A4, Canada;* ⓞ orcid.org/0000-0002-4545-532X
>
> **Grant Walters** − *Department of Electrical and Computer Engineering, University of Toronto, Toronto, Ontario M5S 1A4, Canada*

> **Makhsud I. Saidaminov** − *Department of Electrical and Computer Engineering, University of Toronto, Toronto, Ontario M5S 1A4, Canada; Department of Chemistry and Electrical & Computer Engineering, Centre for Advanced Materials and Related Technologies (CAMTEC), University of Victoria, Victoria V8P 5C2, Canada;* ⓞ orcid.org/0000-0002-3850-666X
>
> **Ziru Huang** − *Department of Electrical and Computer Engineering, University of Toronto, Toronto, Ontario M5S 1A4, Canada;* ⓞ orcid.org/0000-0001-7983-913X
>
> **Koen Bertens** − *Department of Electrical and Computer Engineering, University of Toronto, Toronto, Ontario M5S 1A4, Canada;* ⓞ orcid.org/0000-0002-2701-1397
>
> **Niina Jalarvo** − *Oak Ridge National Laboratory, Oak Ridge, Tennessee 37830, United States;* ⓞ orcid.org/0000-0003-0644-6866

Complete contact information is available at:
https://pubs.acs.org/10.1021/acsnano.0c05179

Notes

The authors declare no competing financial interest.

REFERENCES

(1) Photovoltaic Research, NREL. Best Research-Cell Efficiency Chart, https://www.nrel.gov/pv/cell-efficiency.html (accessed Aug 21, 2019).

(2) Jeon, N. J.; Noh, J. H.; Yang, W. S.; Kim, Y. C.; Ryu, S.; Seo, J.; Seok, S. I. Compositional Engineering of Perovskite Materials for High-Performance Solar Cells. *Nature* **2015**, *517* (7535), 476−480.

(3) Yang, W. S.; Park, B.-W.; Jung, E. H.; Jeon, N. J.; Kim, Y. C.; Lee, D. U.; Shin, S. S.; Seo, J.; Kim, E. K.; Noh, J. H.; Seok, S. I. Iodide Management in Formamidinium-Lead-Halide-Based Perovskite Layers for Efficient Solar Cells. *Science* **2017**, *356*, 1376−1379.

(4) Sahli, F.; Werner, J.; Kamino, B. A.; Bräuninger, M.; Monnard, R.; Paviet-Salomon, B.; Barraud, L.; Ding, L.; Leon, J. J. D.; Sacchetto, D.; Cattaneo, G.; Despeisse, M.; Boccard, M.; Nicolay, S.; Jeangros, Q.; Niesen, B.; Ballif, C. Fully Textured Monolithic Perovskite/Silicon Tandem Solar Cells with 25.2% Power Conversion Efficiency. *Nat. Mater.* **2018**, *17* (9), 820−826.

(5) Tan, H.; Jain, A.; Voznyy, O.; Lan, X.; García de Arquer, F. P.; Fan, J. Z.; Quintero-Bermudez, R.; Yuan, M.; Zhang, B.; Zhao, Y.; Fan, F.; Li, P.; Quan, L. N.; Zhao, Y.; Lu, Z.-H.; Yang, Z.; Hoogland, S.; Sargent, E. H. Efficient and Stable Solution-Processed Planar Perovskite Solar Cells *via* Contact Passivation. *Science* **2017**, *355* (6326), 722−726.

(6) Jung, E. H.; Jeon, N. J.; Park, E. Y.; Moon, C. S.; Shin, T. J.; Yang, T.-Y.; Noh, J. H.; Seo, J. Efficient, Stable and Scalable Perovskite Solar Cells Using Poly(3-Hexylthiophene). *Nature* **2019**, *567* (7749), 511−515.

(7) Saliba, M.; Matsui, T.; Seo, J.-Y.; Domanski, K.; Correa-Baena, J.-P.; Nazeeruddin, M. K.; Zakeeruddin, S. M.; Tress, W.; Abate, A.; Hagfeldt, A.; Grätzel, M. Cesium-Containing Triple Cation Perovskite

Solar Cells: Improved Stability, Reproducibility and High Efficiency. *Energy Environ. Sci.* **2016**, *9* (6), 1989−1997.

(8) Xiao, J.-W.; Liu, L.; Zhang, D.; De Marco, N.; Lee, J.-W.; Lin, O.; Chen, Q.; Yang, Y. The Emergence of the Mixed Perovskites and Their Applications as Solar Cells. *Adv. Energy Mater.* **2017**, *7* (20), 1700491.

(9) Lee, J.-W.; Dai, Z.; Han, T.-H.; Choi, C.; Chang, S.-Y.; Lee, S.-J.; De Marco, N.; Zhao, H.; Sun, P.; Huang, Y.; Yang, Y. 2D Perovskite Stabilized Phase-Pure Formamidinium Perovskite Solar Cells. *Nat. Commun.* **2018**, *9* (1), 1−10.

(10) Bi, D.; Tress, W.; Dar, M. I.; Gao, P.; Luo, J.; Renevier, C.; Schenk, K.; Abate, A.; Giordano, F.; Correa Baena, J.-P.; Decoppet, J.-D.; Zakeeruddin, S. M.; Nazeeruddin, M. K.; Grätzel, M.; Hagfeldt, A. Efficient Luminescent Solar Cells Based on Tailored Mixed-Cation Perovskites. *Sci. Adv.* **2016**, *2* (1), No. e1501170.

(11) Rehman, W.; McMeekin, D. P.; Patel, J. B.; Milot, R. L.; Johnston, M. B.; Snaith, H. J.; Herz, L. M. Photovoltaic Mixed-Cation Lead Mixed-Halide Perovskites: Links between Crystallinity, Photo-Stability and Electronic Properties. *Energy Environ. Sci.* **2017**, *10* (1), 361−369.

(12) Bischak, C. G.; Hetherington, C. L.; Wu, H.; Aloni, S.; Ogletree, D. F.; Limmer, D. T.; Ginsberg, N. S. Origin of Reversible Photoinduced Phase Separation in Hybrid Perovskites. *Nano Lett.* **2017**, *17*, 1028−1033.

(13) Slotcavage, D. J.; Karunadasa, H. I.; McGehee, M. D. Light-Induced Phase Segregation in Halide- Perovskite Absorbers. *ACS Energy Lett.* **2016**, *1*, 1199−1205.

(14) Yoon, S. J.; Draguta, S.; Manser, J. S.; Sharia, O.; Schneider, W. F.; Kuno, M.; Kamat, P. V. Tracking Iodide and Bromide Ion Segregation in Mixed Halide Lead Perovskites during Photoirradiation. *ACS Energy Lett.* **2016**, *1*, 290−296.

(15) Herz, L. M. How Lattice Dynamics Moderate the Electronic Properties of Metal-Halide Perovskites. *J. Phys. Chem. Lett.* **2018**, *9* (23), 6853−6863.

(16) Caselli, V. M.; Fischer, M.; Meggiolaro, D.; Mosconi, E.; De Angelis, F.; Stranks, S. D.; Baumann, A.; Dyakonov, V.; Hutter, E. M.; Savenije, T. J. Charge Carriers Are Not Affected by the Relatively Slow-Rotating Methylammonium Cations in Lead Halide Perovskite Thin Films. *J. Phys. Chem. Lett.* **2019**, *10*, 5128−5134.

(17) Bakulin, A. A.; Selig, O.; Bakker, H. J.; Rezus, Y. L.A.; Muller, C.; Glaser, T.; Lovrincic, R.; Sun, Z.; Chen, Z.; Walsh, A.; Frost, J. M.; Jansen, T. L. C. Real-Time Observation of Organic Cation Reorientation in Methylammonium Lead Iodide Perovskites. *J. Phys. Chem. Lett.* **2015**, *6*, 3663−3669.

(18) Gélvez-Rueda, M. C.; Cao, D. H.; Patwardhan, S.; Renaud, N.; Stoumpos, C. C.; Schatz, G. C.; Hupp, J. T.; Farha, O. K.; Savenije, T. J.; Kanatzidis, M. G.; Grozema, F. C. Effect of Cation Rotation on Charge Dynamics in Hybrid Lead Halide Perovskites. *J. Phys. Chem. C* **2016**, *120* (30), 16577−16585.

(19) Zhu, X.-Y.; Podzorov, V. Charge Carriers in Hybrid Organic−Inorganic Lead Halide Perovskites Might Be Protected as Large Polarons. *J. Phys. Chem. Lett.* **2015**, *6* (23), 4758−4761.

(20) Joshi, P. P.; Maehrlein, S. F.; Zhu, X. Dynamic Screening and Slow Cooling of Hot Carriers in Lead Halide Perovskites. *Adv. Mater.* **2019**, *31*, 1803054.

(21) Chen, T.; Chen, W.-L.; Foley, B. J.; Lee, J.; Ruff, J. P. C.; Ko, J. Y. P.; Brown, C. M.; Harriger, L. W.; Zhang, D.; Park, C.; Yoon, M.; Chang, Y.-M.; Choi, J. J.; Lee, S.-H. Origin of Long Lifetime of Band-Edge Charge Carriers in Organic−Inorganic Lead Iodide Perovskites. *Proc. Natl. Acad. Sci. U. S. A.* **2017**, *114* (29), 7519−7524.

(22) Gallop, N. P.; Selig, O.; Giubertoni, G.; Bakker, H. J.; Rezus, Y. L. A.; Frost, J. M.; Jansen, T. L. C.; Lovrincic, R.; Bakulin, A. A. Rotational Cation Dynamics in Metal Halide Perovskites: Effect on Phonons and Material Properties. *J. Phys. Chem. Lett.* **2018**, *9* (20), 5987−5997.

(23) Bonn, M.; Miyata, K.; Hendry, E.; Zhu, X.-Y. Role of Dielectric Drag in Polaron Mobility in Lead Halide Perovskites. *ACS Energy Lett.* **2017**, *2* (11), 2555−2562.

(24) Frost, J. M.; Butler, K. T.; Brivio, F.; Hendon, C. H.; van Schilfgaarde, M.; Walsh, A. Atomistic Origins of High-Performance in

Hybrid Halide Perovskite Solar Cells. *Nano Lett.* **2014**, *14* (5), 2584−2590.

(25) Walsh, A. Principles of Chemical Bonding and Band Gap Engineering in Hybrid Organic−Inorganic Halide Perovskites. *J. Phys. Chem. C* **2015**, *119*, 5755−5760.

(26) Umari, P.; Mosconi, E.; De Angelis, F. Infrared Dielectric Screening Determines the Low Exciton Binding Energy of Metal-Halide Perovskites. *J. Phys. Chem. Lett.* **2018**, *9* (3), 620−627.

(27) Wright, A. D.; Verdi, C.; Milot, R. L.; Eperon, G. E.; Pérez-Osorio, M. A.; Snaith, H. J.; Giustino, F.; Johnston, M. B.; Herz, L. M. Electron−Phonon Coupling in Hybrid Lead Halide Perovskites. *Nat. Commun.* **2016**, *7* (1), 11755.

(28) Grechko, M.; Bretschneider, S. A.; Vietze, L.; Kim, H.; Bonn, M. Vibrational Coupling between Organic and Inorganic Sublattices of Hybrid Perovskites. *Angew. Chem., Int. Ed.* **2018**, *57* (41), 13657−13661.

(29) Chen, T.; Foley, B. J.; Ipek, B.; Tyagi, M.; Copley, J. R. D.; Brown, C. M.; Choi, J. J.; Lee, S.-H. Rotational Dynamics of Organic Cations in the $CH_3NH_3PbI_3$ Perovskite. *Phys. Chem. Chem. Phys.* **2015**, *17* (46), 31278−31286.

(30) Schuck, G.; Lehmann, F.; Ollivier, J.; Mutka, H.; Schorr, S. Influence of Chloride Substitution on the Rotational Dynamics of Methylammonium in $MAPbI_{3-x}Cl_x$ Perovskites. *J. Phys. Chem. C* **2019**, *123*, 11436.

(31) Li, J.; Bouchard, M.; Reiss, P.; Aldakov, D.; Pouget, S.; Demadrille, R.; Aumaitre, C.; Frick, B.; Djurado, D.; Rossi, M.; Rinke, P. Activation Energy of Organic Cation Rotation in $CH_3NH_3PbI_3$ and $CD_3NH_3PbI_3$: Quasi-Elastic Neutron Scattering Measurements and First-Principles Analysis Including Nuclear Quantum Effects. *J. Phys. Chem. Lett.* **2018**, *9* (14), 3969−3977.

(32) Leguy, A. M. A.; Frost, J. M.; McMahon, A. P.; Sakai, V. G.; Kockelmann, W.; Law, C.; Li, X.; Foglia, F.; Walsh, A.; O'Regan, B. C.; Nelson, J.; Cabral, J. T.; Barnes, P. R. F. The Dynamics of Methylammonium Ions in Hybrid Organic−Inorganic Perovskite Solar Cells. *Nat. Commun.* **2015**, *6*, 7124.

(33) Swainson, I. P.; Stock, C.; Parker, S. F.; Van Eijck, L.; Russina, M.; Taylor, J. W. From Soft Harmonic Phonons to Fast Relaxational Dynamics in CH 3 NH 3 PbBr 3. *Phys. Rev. B: Condens. Matter Mater. Phys.* **2015**, *92* (10), 100303.

(34) Saidaminov, M. I.; Kim, J.; Jain, A.; Quintero-Bermudez, R.; Tan, H.; Long, G.; Tan, F.; Johnston, A.; Zhao, Y.; Voznyy, O.; Sargent, E. H. Suppression of Atomic Vacancies *via* Incorporation of Isovalent Small Ions to Increase the Stability of Halide Perovskite Solar Cells in Ambient Air. *Nature Energy* **2018**, *3* (8), 648−654.

(35) Gong, X.; Voznyy, O.; Jain, A.; Liu, W.; Sabatini, R.; Piontkowski, Z.; Walters, G.; Bappi, G.; Nokhrin, S.; Bushuyev, O.; Yuan, M.; Comin, R.; McCamant, D.; Kelley, S. O.; Sargent, E. H. Electron−Phonon Interaction in Efficient Perovskite Blue Emitters. *Nat. Mater.* **2018**, *17* (6), 550−556.

(36) Zaccai, G. How Soft Is a Protein? A Protein Dynamics Force Constant Measured by Neutron Scattering. *Science* **2000**, *288*, 1604−1607.

(37) Chen, T.; Foley, B. J.; Park, C.; Brown, C. M.; Harriger, L. W.; Lee, J.; Ruff, J.; Yoon, M.; Choi, J. J.; Lee, S.-H. Entropy-Driven Structural Transition and Kinetic Trapping in Formamidinium Lead Iodide Perovskite. *Science Advances* **2016**, *2*, e1601650.

(38) Binek, A.; Hanusch, F. C.; Docampo, P.; Bein, T. Stabilization of the Trigonal High-Temperature Phase of Formamidinium Lead Iodide. *J. Phys. Chem. Lett.* **2015**, *6*, 1249−1253.

(39) Weller, M. T.; Weber, O. J.; Frost, J. M.; Walsh, A. Cubic Perovskite Structure of Black Formamidinium Lead Iodide, A-[HC(NH2)2]PbI3, at 298 K. *J. Phys. Chem. Lett.* **2015**, *6*, 3209−3212.

(40) Bee, M. *Quasielastic Neutron Scattering: Principles and Applications in Solid State Chemistry, Biology and Materials Sciente*; IOP Publishing Ltd: Bristol, England, 1988.

(41) Taylor, V. C. A.; Tiwari, D.; Duchi, M.; Donaldson, P. M.; Clark, I. P.; Fermin, D. J.; Oliver, T. A. A. Investigating the Role of the Organic Cation in Formamidinium Lead Iodide Perovskite Using Ultrafast Spectroscopy. *J. Phys. Chem. Lett.* **2018**, *9* (4), 895−901.

(42) Petrov, A. A.; Goodilin, E. A.; Tarasov, A. B.; Lazarenko, V. A.; Dorovatovskii, P. V.; Khrustalev, V. N. Formamidinium Iodide: Crystal Structure and Phase Transitions. *Acta Crystallographica Section E* **2017**, *73*, 569−572.

(43) Ren, Y.; Oswald, I. W. H.; Wang, X.; McCandless, G. T.; Chan, J. Y. Orientation of Organic Cations in Hybrid Inorganic−Organic Perovskite CH₃NH₃PbI₃ from Subatomic Resolution Single Crystal Neutron Diffraction Structural Studies. *Cryst. Growth Des.* **2016**, *16* (5), 2945−2951.

(44) Saidaminov, M. I.; Williams, K.; Wei, M.; Johnston, A.; Quintero-Bermudez, R.; Vafaie, M.; Pina, J. M.; Proppe, A. H.; Hou, Y.; Walters, G.; Kelley, S. O.; Tisdale, W. A.; Sargent, E. H. Multi-Cation Perovskites Prevent Carrier Reflection from Grain Surfaces. *Nat. Mater.* **2020**, *19* (4), 412−418.

(45) Selig, O.; Sadhanala, A.; Müller, C.; Lovrincic, R.; Chen, Z.; Rezus, Y. L. A.; Frost, J. M.; Jansen, T. L. C.; Bakulin, A. A. Organic Cation Rotation and Immobilization in Pure and Mixed Methyl-ammonium Lead-Halide Perovskites. *J. Am. Chem. Soc.* **2017**, *139* (11), 4068−4074.

(46) Jiang, Q.; Zhao, Y.; Zhang, X.; Yang, X.; Chen, Y.; Chu, Z.; Ye, Q.; Li, X.; Yin, Z.; You, J. Surface Passivation of Perovskite Film for Efficient Solar Cells. *Nat. Photonics* **2019**, *13* (7), 460−466.

(47) Zhu, H.; Miyata, K.; Fu, Y.; Wang, J.; Joshi, P. P.; Niesner, D.; Williams, K. W.; Jin, S.; Zhu, X.- Y. Screening in Crystalline Liquids Protects Energetic Carriers in Hybrid Perovskites. *Science* **2016**, *353*, 1409−1413.

(48) Even, J.; Pedesseau, L.; Katan, C. Analysis of Multivalley and Multibandgap Absorption and Enhancement of Free Carriers Related to Exciton Screening in Hybrid Perovskites. *J. Phys. Chem. C* **2014**, *118*, 11566−11572.

(49) Soufiani, A. M.; Huang, F.; Reece, P.; Sheng, R.; Ho-Baillie, A.; Green, M. A. Polaronic Exciton Binding Energy in Iodide and Bromide Organic-Inorganic Lead Halide Perovskites. *Appl. Phys. Lett.* **2015**, *107* (23), 231902.

(50) Elliott, R. J. Intensity of Optical Absorption by Excitons. *Phys. Rev.* **1957**, *108* (6), 1384−1389.

(51) Davies, C. L.; Filip, M. R.; Patel, J. B.; Crothers, T. W.; Verdi, C.; Wright, A. D.; Milot, R. L.; Giustino, F.; Johnston, M. B.; Herz, L. M. Bimolecular Recombination in Methylammonium Lead Triiodide Perovskite Is an Inverse Absorption Process. *Nat. Commun.* **2018**, *9* (1), 1−9.

(52) Yang, Y.; Yang, M.; Li, Z.; Crisp, R.; Zhu, K.; Beard, M. C. Comparison of Recombination Dynamics in CH3NH3PbBr3 and CH3NH3PbI3 Perovskite Films: Influence of Exciton Binding Energy. *J. Phys. Chem. Lett.* **2015**, *6*, 4688−4692.

(53) Saidaminov, M. I.; Abdelhady, A. L.; Murali, B.; Alarousu, E.; Burlakov, V. M.; Peng, W.; Dursun, I.; Wang, L.; He, Y.; Maculan, G.; Goriely, A.; Wu, T.; Mohammed, O. F.; Bakr, O. M. High-Quality Bulk Hybrid Perovskite Single Crystals within Minutes by Inverse Temper-ature Crystallization. *Nat. Commun.* **2015**, *6*, 7586.

(54) Mamontov, E.; Herwig, K. W. A Time-of-Flight Backscattering Spectrometer at the Spallation Neutron Source, BASIS. *Rev. Sci. Instrum.* **2011**, *82*, 085109.

(55) Arnold, O.; Bilheux, J. C.; Borreguero, J. M.; Buts, A.; Campbell, S. I.; Chapon, L.; Doucet, M.; Draper, N.; Ferraz Leal, R.; Gigg, M. A.; Lynch, V. E.; Markvardsen, A.; Mikkelson, D. J.; Mikkelson, R. L.; Miller, R.; Palmen, K.; Parker, P.; Passos, G.; Perring, T. G.; Peterson, P. F.; Ren, S.; Reuter, M. A.; Savici, A. T.; Taylor, J. W.; Taylor, R. J.; Tolchenov, R.; Zhou, W.; Zikovsky, J. Mantid—Data Analysis and Visualization Package for Neutron Scattering and μ SR Experiments. *Nucl. Instrum. Methods Phys. Res., Sect. A* **2014**, *764*, 156−166.

(56) Azuah, R. T.; Kneller, L. R.; Qiu, Y.; Tregenna-Piggott, P. L. W.; Brown, C. M.; Copley, J. R. D.; Dimeo, R. M. DAVE: A Comprehensive Software Suite for the Reduction, Visualization, and Analysis of Low Energy Neutron Spectroscopic Data. *J. Res. Natl. Inst. Stand. Technol.* **2009**, *114* (6), 341.

(57) Character tables for chemically important point groups, http://symmetry.jacobs-university.de/ (accessed Jul 22, 2019).